Nonlinear Dynamics manuscript No.
https://doi.org/10.1007/s11071-025-11032-3

Parameter Identification of a Nonlinear Vertical Axis Rotating Machine through Reduced Order Modeling and Data Assimilation

Sima Rishmawi · Ludivine Moyne · Souheil Serroud · Sebastian Rodriguez · Francisco Chinesta · Oguzhan Tuysuz · Frédérick P. Gosselin

Received: 13 December 2024 / Accepted: 18 February 2025

Abstract One challenge in modeling nonlinear dynamic systems involves the uncertainty associated with certain parameters that cannot be directly measured or estimated, along with the complexity of incorporating all relevant physical phenomena into a mathematical model without increasing computational cost. A hybrid twin represents an advanced modeling approach that combines the system's physics-based mathematical model with the empirical data collected from the real-world system, using data assimilation. This strategy enhances the accuracy and reliability of both estimating the system's unknown parameters and predicting its overall behavior. Further improvements are achieved by using a reduced-order model, which significantly lowers the computational burden of the entire procedure. In this study, we construct a surrogate model for a Vertical Axis Rotating Machine (VARM) by deploying sparse Proper Generalized Decomposition (sPGD). The model is parametrized in terms of the machine's unidentified parameters, and we apply the Harmonic-Modal Hybrid (HMH) Frequency Approach to solve for sparse scenarios creating the library of solutions. This is then combined with the Levenberg-Marquardt optimization technique to identify the unknown parameters using the measured shaft displacements of an experimental rig of the machine. The results demonstrate that this method is effective for parameter estimation in complex nonlinear systems and allows for fast computations, whether the unknown force function is specified explicitly or presumed. Precisely estimating a system's parameters can serve as a crucial indicator for scheduling maintenance or predicting failures.

Keywords Nonlinear Dynamics · Model Order Reduction · sPGD · Data Assimilation · Levenberg-Marquardt · Inverse Analysis

S. Rishmawi (✉) · L. Moyne · S. Serroud · F. P. Gosselin
Multi-scale Mechanics Laboratory (LM2), École Polytechnique de Montréal
2500 Chemin de Polytechnique, Montréal, H3T 1J4, QC, Canada
E-mail: sima-2.rishmawi@polymtl.ca

O. Tuysuz
Virtual Manufacturing Research Laboratory, École Polytechnique de Montréal
2500 Chemin de Polytechnique, Montréal, H3T 1J4, QC, Canada

S. Rodriguez · F. Chinesta
PIMM Laboratory, Arts et Métiers Institute of Technology, CNRS, Cnma, HESAM Université
151 Boulevard de l'Hôpital, 75013, Paris, France

1 Introduction

Grey-box modeling combines elements of white-box models, which are formulated with detailed insights into system physics, and black-box models, which rely entirely on data. The grey-box method strikes a balance between precision and flexibility [1,2]. It is especially effective when the differential equations that govern the behavior of the system are known, but some parameters in these equations are difficult to identify; then measured data can be used to estimate these unknown features. According to this concept, a grey-box model aligns with the Hybrid Twins framework presented by Chinesta et al. in Ref. [3]. This framework enhances a physics-based model by incorporating empirical data to create a virtual equivalent of a real or anticipated physical system.

Rotating machines are an example of systems with incomplete knowledge. Typically, these machines experience vibrations caused by both the shaft's and sup-

ports' flexibility [4–6]. Shaft flexibility is usually captured using models for bending and torsion of beams, while modeling the supports proves more challenging, due to the diverse physical phenomena involved, including bearing physics with hydrodynamic lubrication, rolling components, thermal influences, and mounting compliance. The nonlinearly coupled multi-physical characteristics of the supports necessitate simulations that depend on parameters that are challenging to quantify, thereby making simulations difficult to achieve. This is particularly true for machines with a vertical axis of rotation. Conversely, in horizontal axis machines, the calculation of bearing reaction forces is based on the static radial loads due to the rotor's dead weight [7,8].

Extensive research has explored how bearing forces affect rotor dynamics. Bearings, often seen as localized rotor-stator interactions with specific damping and stiffness, generate reaction forces. These properties are crucial for modeling the shaft forces, but are influenced by various factors and are typically nonlinear in vertical machines, making them difficult to quantify [5,8,9].

Researchers have developed three primary categories of approaches to evaluate bearing forces and coefficients in rotating machinery. The first category involves the use of sensor data or experimental measurements to determine unknown bearing parameters in horizontal and vertical machines [10–12]. The second approach is based on solving the Navier-Stokes equations. It is used to calculate the coefficients of journal bearings. This is generally accomplished using computer software programs, such as the one provided in Ref. [13]. The third approach, which is commonly used, models the bearing forces as functions of the lateral displacements and velocities of the shaft in the plane perpendicular to its axis of rotation involving parameters that require identification [14].

When addressing a differential equation with one or more unknown parameters, three strategies are available: (1) A cautious approach involves determining the parameter's value before solving the equation, for instance, through sensor measurements if feasible. (2) Solving the equation repeatedly with varying parameter values, and choosing the one providing the closest approximation of the response. (3) Solving the equation comprehensively for an entire range of the unknown parameter(s), with the range being refined according to the problem's specifications, resulting in a parametrized solution [15].

Proper Generalized Decomposition (PGD) is an effective method for crafting a parametrized solution to differential equations. Initially, PGD was introduced as an *a priori* intrusive Model Order Reduction (MOR) projection-based technique that yields an economical low-rank approximation of the solution to a global space-time problem. The notion of a parametrized solution emerged when Chinesta et al. expanded PGD to incorporate system parameters alongside space and time [16–18]. PGD aims at achieving a distinct representation of an unknown field referred to as a finite sum decomposition. In the context of problems involving n_p parameters, each summation term (enrichment step) within the PGD representation consists of a set of n_p one-dimensional functions, which are simpler to resolve compared to dealing with a single function of n_p dimensions.

Another way to apply PGD is through an *a posteriori*, non-intrusive method. This involves performing an offline calculation with a high-fidelity model and then using the sparse Proper Generalized Decomposition (sPGD) technique to compress the results into a parametrized reduced order model (ROM) [19]. The sPGD technique was initially introduced in Refs. [20, 21]. It offers benefits such as handling unstructured datasets, maintaining robustness in high-dimensional spaces, and not requiring an extensive dataset for convergence.

In Ref. [22], Rishmawi et al. introduced an alternative technique for conducting the offline sPGD calculations. This approach leverages a nonlinear global space-frequency solver to iteratively construct a low-rank solution for a nonlinear differential equation, employing the Harmonic-Modal Hybrid (HMH) method as detailed in Ref. [23]. Implementing this method during the offline calculation stage of the sPGD ensures precise outcomes while significantly reducing the computational cost.

In the realm of data assimilation methods, Static Data-Driven Application Systems (SDDAS) are characterized by models that gather data *a priori* through sensors from a physical source; hence, data is not continuously fed into the system for real-time updates [3,24]. This collected data is subsequently employed to solve an optimization problem, where it serves to estimate unknown parameter values within a differential equation while minimizing the disparity between the observed data and the simulated response. The Levenberg-Marquardt (LM) algorithm serves as an optimization method to solve such problems. Originating from early 1960s, LM was designed to address nonlinear least square problems. It merges the advantageous features of the Gradient-Descent and Gauss-Newton optimization methods, specifically convergence and rapidity [25]. For comprehensive derivations of these techniques and their integration within the LM algorithm, the reader is advised to refer to Ref. [25], where a suggested numerical implementation with codes can be found. It is advisable to

integrate LM with sPGD because the LM algorithm's costliest step is the computation of the Jacobian matrix, a task that is performed automatically by the sPGD algorithm, storing the Jacobians within the sPGD library, thereby accelerating the optimization procedure. The most relevant example in the literature involves the integration of intrusive PGD with the LM optimization method to determine the optimal parameters for a 2D thermal problem [15]. This method was broadened to incorporate sPGD in Ref. [19], where it was used to create a hybrid twin of a Resin Transfer Molding (RTM) process to ensure correct filling.

Here we introduce a parametrized Reduced-Order-Model (ROM) for a nonlinear Vertical Axis Rotating Machine (VARM)using a surrogate sPGD model in conjunction with the LM optimization method for inverse analysis. This approach is used to identify unknown parameters essential to characterizing the nonlinear bearing forces on the VARM shaft within a grey-box hybrid twin framework. To accelerate the offline computations needed for constructing the sPGD solution library, we employ the HMH global nonlinear space-frequency solver. While all techniques applied in this method have been previously developed and validated individually, they have never been combined in this manner to create a dependable hybrid twin for such a system.

This article is organized as follows: Section 2 outlines the overall framework of the developed methodology by describing the steps where each numerical technique is employed, and explaining how they are linked to create a hybrid twin. Section 3 presents the newly designed and tested vertical axis rotating machine. The findings of this research are presented in Section 4. Lastly, the concluding remarks and suggestions for future research directions are provided in Section 5.

2 General Methodology

Figure 1 illustrates the three primary stages of the proposed method to develop a hybrid twin of a vibrating system using a grey-box framework. The first step involves determining the unknown parameters and estimating a plausible range for each of them. Then a set of sparse parameter scenarios is generated using a Latin hypercube. Following this, the HMH method is employed to calculate the system's response as a function of the unknown parameters for each one of those scenarios. By executing the solver multiple times with various sets of unknown parameters within their expected ranges, we generate a sparse dataset. This dataset is subsequently used as input for an sPGD algorithm, resulting in a library of solutions for the parametrized problem. The second step entails recording data from the physical entity of the system. Subsequently, the final step consists of leveraging the collected data to derive the optimal values for the unknown parameters that reduce the discrepancy between the observed and simulated shaft displacements. This is achieved by employing the LM optimization technique to develop a comprehensive model of the system at hand. The sPGD solution library accelerates the LM optimization technique considerably, as it can promptly provide the solution for any set of parameters which is required in these iterative processes, thereby obviating the need for time integration and other computationally intensive methods. The thoroughly developed mathematical model can be used for future system monitoring and control, as well as maintenance planning and fault detection. Naturally, the approach should be customized to meet the requirements of the specific models under consideration.

2.1 White-Box Model

This part of the methodology describes the development of a surrogate model based on pre-computed scenarios aimed at rapidly predicting the parameterized dynamic response of a system. Initially, a Latin hypercube sampling generates n_s random scenarios, each consisting of a specific combination of n_p unknown parameter values within their defined ranges as follows:

$$\mathbf{P}_{LHC} = \begin{bmatrix} p_1^1 & p_2^1 & \cdots & p_{n_p}^1 \\ p_1^2 & p_2^2 & \cdots & p_{n_p}^2 \\ \vdots & \vdots & \ddots & \vdots \\ p_1^{n_s} & p_2^{n_s} & \cdots & p_{n_p}^{n_s} \end{bmatrix}. \tag{1}$$

Here, p_i^j denotes the i^{th} parameter within the j^{th} scenario. Each scenario in the matrix $\mathbf{P}_{LHC}$, generates a distinct system response that must be calculated explicitly for every scenario. To achieve reliable and rapid computations, we employ the HMH solver [22] to solve for those scenarios.

The iterative HMH solver relies on modal basis analysis in the frequency domain to address a nonlinear Partial Differential Equation (PDE) without requiring a time integration scheme. Its core concept involves employing the fixed-point Alternating Frequency Time method (AFT) [26], in which the Fast Fourier Transform ($\mathcal{FFT}$) is used on the linear segment of the equation of motion to convert it into the frequency domain, where the initial response is computed in the first iteration. This response is then converted back to the time domain to determine the nonlinear force. In subsequent iterations, the nonlinear force component is calculated using the previously obtained response, represented as

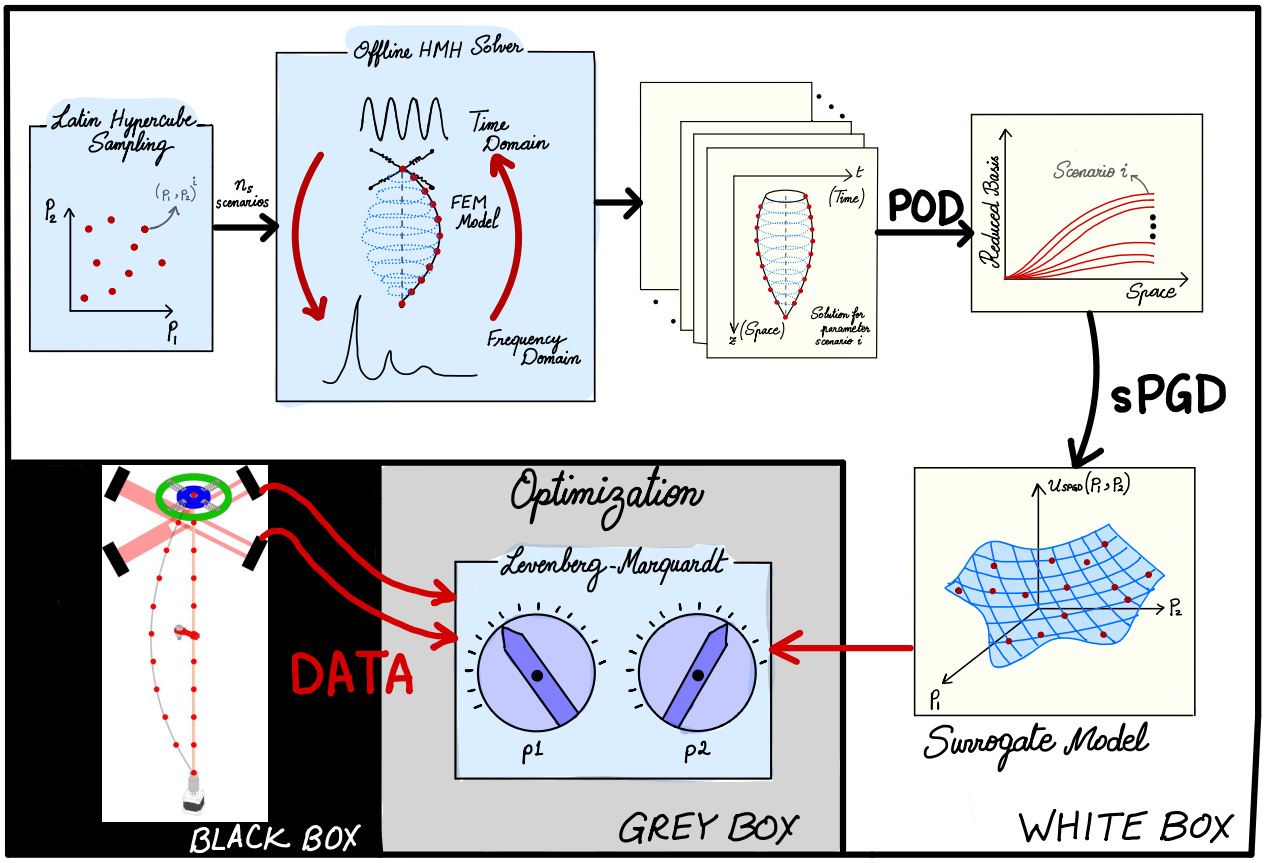

Fig. 1 A diagram reflecting the overall outlined methodology, detailing each step involved in the white, black, and grey-box models, along with their respective inputs and outputs, illustrating their interconnection in forming the comprehensive model. To enhance clarity and visibility, the example focuses on optimizing two unknown parameters, though this approach can be expanded to optimize several parameters.

a numerical vector. This vector undergoes $\mathcal{FFT}$ again, facilitating the response calculation for the next iteration. It is essential to note that in the frequency domain, the solution is explicit. This implies that when employing modal basis analysis, the equations are entirely decoupled in the frequency domain.

Considering an arbitrary nonlinear differential equation of the form:

$$\mathbf{M}\{\ddot{\vec{\mathbf{u}}}\} + \mathbf{C}\{\dot{\vec{\mathbf{u}}}\} + \mathbf{K}\{\vec{\mathbf{u}}\} - \{\overrightarrow{\mathbf{R}(\{\vec{\mathbf{u}}\})}\} = \{\vec{\mathbf{f}}\}, \qquad (2)$$

where the notation $\{\ddot{\cdot}\}$ and $\{\dot{\cdot}\}$ represent the second and first derivatives with respect to time, respectively, $\mathbf{M}$, $\mathbf{C}$, and $\mathbf{K}$ are general mass, damping, and stiffness matrices of an arbitrary vibration system, respectively, and $\{\overrightarrow{\mathbf{R}(\{\vec{\mathbf{u}}\})}\}$ is a nonlinear contribution that depends on $\{\vec{\mathbf{u}}\}$, then the aforementioned approach is based on calculating the nonlinear term from the solution at the previous iteration and considering it as an extra loading as follows:

$$\mathbf{M}\{\ddot{\vec{\mathbf{u}}}\} + \mathbf{C}\{\dot{\vec{\mathbf{u}}}\} + \mathbf{K}\{\vec{\mathbf{u}}\} = \{\overrightarrow{\mathbf{R}(\{\overrightarrow{\mathbf{u}^-}\})}\} + \{\vec{\mathbf{f}}\}, \qquad (3)$$

where $\{\overrightarrow{\mathbf{u}^-}\}$ corresponds to the time dependent solution calculated at the previous iteration. Now, $\mathcal{FFT}$ can be directly applied to the right side as well as the left side [22,23,27], to find the solution in the frequency domain.

Typically solving dynamic equations in terms of space and time, the HMH solver results in n_s solution matrices with rows corresponding to the degrees of freedom in space and columns corresponding to the time steps. Due to the complexity of creating a surrogate model based on those matrices using sPGD, as interpolation becomes too intricate, we reduce the rank of these matrices by projecting them onto a reduced basis derived from Proper Orthogonal Decomposition (POD) [28,29]. Thus, Singular Value Decomposition (SVD) is applied to a snapshot matrix formed by concatenating the n_s matrices obtained during the initial offline computation

phase with the HMH solver. The snapshot matrix can be defined as:

$$\mathtt{U} = [\mathbf{U_1}^T, \cdots, \mathbf{U_{n_s}}^T], \tag{4}$$

where $\mathbf{U_i}$ is the solution matrix corresponding to scenario i having a dimension of $n_{DOF} \times n_t$, making the total dimension of $\mathtt{U}$ $n_t \times n_s n_{DOF}$. By applying SVD to the snapshot matrix $\mathtt{U}$, the first few temporal modes can be extracted to form a temporal reduced basis $\mathcal{R}_t$ with the dimension of $n_t \times m_d$, where n_t is the number of time steps and m_d denotes the number of selected modes. The temporal reduced basis $\mathcal{R}_t$ is used to project each complete solution matrix onto the reduced basis, as shown below:

$$\mathcal{U}_i = \mathbf{U}_i \mathcal{R}_t, \tag{5}$$

where $\mathcal{U}_i$ represents the reduced-order portrayal of $\mathbf{U}_i$ and has dimensions of $n_{DOF} \times m_d$ instead of $n_{DOF} \times n_t$, making it significantly easier to manage. The number of selected modes, m_d, is influenced by the level of correlation within the data set. A greater correlation results in fewer modes that need to be extracted.

The concluding phase of this stage involves developing a surrogate model with sPGD which offers a parameterized solution for the problem [20]. The matrix $\mathcal{U}$ can be represented as a function of the n_p unknown parameters according to the sPGD formulation below:

$$\mathcal{U}(p_1, p_2, \cdots, p_{n_p}) = \sum_{k=1}^{M} F_1^k(p_1) F_2^k(p_2) \cdots F_{n_p}^k(p_{n_p}), \tag{6}$$

where M is the number of enrichment steps needed to obtain an acceptable approximation of $\mathcal{U}$ using sPGD. So by defining the functions $F_j^k(\eta)$ we can obtain the solution $\mathcal{U}$ for any combination of the n_p parameters instantaneously. The functions $F_j^k(\eta)$ are expressed as:

$$F_j^k(\eta) = \{N_j^k(\eta)\}^T \{\overrightarrow{\mathbf{a_j}}\}, \tag{7}$$

In this context, $N_j^k(\eta)$ represents a function chosen for interpolation purposes, with j defined as the number of control points [30]. The vector $\{\overrightarrow{\mathbf{a_j}}\}$ contains constant nodal values computed via the sPGD algorithm.

At this stage, a library of solutions is compiled for any parameter combination within the previously defined ranges, encapsulating current knowledge from physics. It is important to highlight that once the response $\mathcal{U}_i$ is computed for a specified set of parameters using the sPGD surrogate model, it must be projected back onto the full basis using the following equation to obtain the complete system solution:

$$\mathbf{U}_i = \mathcal{U}_i \mathcal{R}_t^T. \tag{8}$$

2.2 Black-box Model

A physical entity of the system being studied is necessary at this step. Sensors can be used to gather data from the setup across different operational scenarios, which are chosen according to the problem's characteristics. While kinematic data is commonly collected, other types of data might also be relevant. Should the measured quantity not precisely represent the system's response, an extra step is needed to compute the response from the data to facilitate a comparison with the simulated response.

2.3 Grey-box Model (Hybrid Twin)

This stage solves an optimization problem that estimates the values of the unknown parameters of the system based on the collected data. The optimization problem can be defined as:

$$\{\overrightarrow{\hat{\mathbf{p}}}\} = \underset{p_1, p_2, \cdots, p_{n_p}}{\operatorname{argmin}} \; \mathcal{L}_2 + \mathcal{L}_1, \tag{9}$$

where

$$\mathcal{L}_2 = \left\| \tilde{\mathcal{U}} - \mathcal{U}(p_1, p_2, \cdots, p_{n_p}) \right\|_2, \tag{10}$$

$$\mathcal{L}_1 = \lambda \left\| p_1, p_2, \cdots, p_{n_p} \right\|_1. \tag{11}$$

Equation (9) determines the vector of optimized parameters $\{\overrightarrow{\hat{\mathbf{p}}}\}$ by minimizing a loss function, which includes the $\mathcal{L}_2$ norm reflecting the least squares error between the simulated response $\mathcal{U}$ and the measured data $\tilde{\mathcal{U}}$. In addition to the $\mathcal{L}_1$ norm that features a term promoting sparsity. The parameter $\lambda \geq 0$ is a hyper-parameter used to weight the significance of sparsity. The sparsity term is crucial in identifying the parameters that significantly impact the solution, enabling discarding insignificant terms and thus simplifying the problem.

Numerous optimization techniques that solve such problems are available in the literature; however, we chose the Levenberg-Marquardt (LM) algorithm because it does not necessitate time-integration, converges rapidly, and addresses the limitations of other methods by integrating both the Gradient-Descent and Gauss-Newton methods.

To prevent being trapped in a local minimum, the optimization procedure is executed in τ independent trials, each initiated with a different random set of unknown parameters. The set of parameters that results in the lowest value of the loss function is then chosen as the solution. We further enhanced the technique by applying a Monte Carlo simulation which executes the

Fig. 2 A photograph of the VARM built and tested at Polytechnique Montréal. For reference, the shaft length from the upper bearing to the lower bearing is 850 mm.

aforementioned optimization procedure n_{MC} times, averaging the results for each parameter. This method ensures that the results closely reflect reality and avoids local minima. Such comprehensive calculations can be performed without compromising on computational resources because the entire process uses the sPGD library, which pre-computes the Jacobian matrix and extracts solutions for various parameter sets in milliseconds. According to Rishmawi et al. [22], the duration required to obtain the system's response for a specific parameter set from the sPGD library is 99% less compared to solving the system for the same parameter set using high-fidelity methods like Newton-Raphson at the expense of performing large and expensive offline calculations which are done once and for all. Depending on computational capabilities, the online computation time can range from $1e-5$ to $1e-3$ s. Thus, the LM algorithm is able to achieve convergence through an iterative parameter identification process in real-time.

It is important to note that it is highly recommended to normalize the parameters to ranges between -1 and 1, or 0 and 1, based on their physical significance, to ensure more accurate approximations during the LM optimization process.

3 Case Study: Vertical Axis Rotating Machine

In this section, we present the VARM as a case study to validate the developed methodology. Figure 2 shows a photograph of the machine built and tested at Polytechnique Montréal.

3.1 VARM Experimental Setup

Figure 3a presents a 3D illustration of a VARM designed and built to test hybrid twins. This device features a vertical shaft and experiences nonlinear forces arising from shaft displacements at the bearings, which are typically challenging to quantify. To address this, a long and thin bronze shaft measuring 850 mm in length with a Young's modulus of 110.3 GPa was mounted between two distinct bearings: a fixed flanged miniature pillow block mounted MFL4 ball bearing at the lower end of the shaft, and an Uxcell R4A-2RS deep groove ball bearing housed in a 3D printed structure composed of Polylactic Acid (PLA) plastic at the upper end. This upper bearing was made flexible by mounting it on four perpendicular tension-compression springs. The springs are identical, constructed from a 1.702 mm gauge stainless steel wire, featuring an outer diameter of 18.3 mm, and an unstretched length of 50.8 mm and consisting of 8 coils. To simulate unbalances and imperfections, a mass was asymmetrically attached to the beam using a 3D printed PLA attachment to create a rotating unbalance. The whole setup is mounted on an NI ISM-7402 stepper motor.

Two Keyence IG-028 Laser micrometers were positioned perpendicular to each other in each direction of motion, to measure the displacement of a point located at one-tenth of the shaft's full length from the top bearing. This point, as will become evident in subsequent steps, aligns with the second node on the shaft, which will be divided into 10 elements using 11 nodes, as illustrated in Figure 3b. These sensors have a gate size of 28 mm, with precision ranging from 0.03 mm to 0.17 mm based on the spacing between the transmitter and receiver, which can reach up to 1500 mm. In this

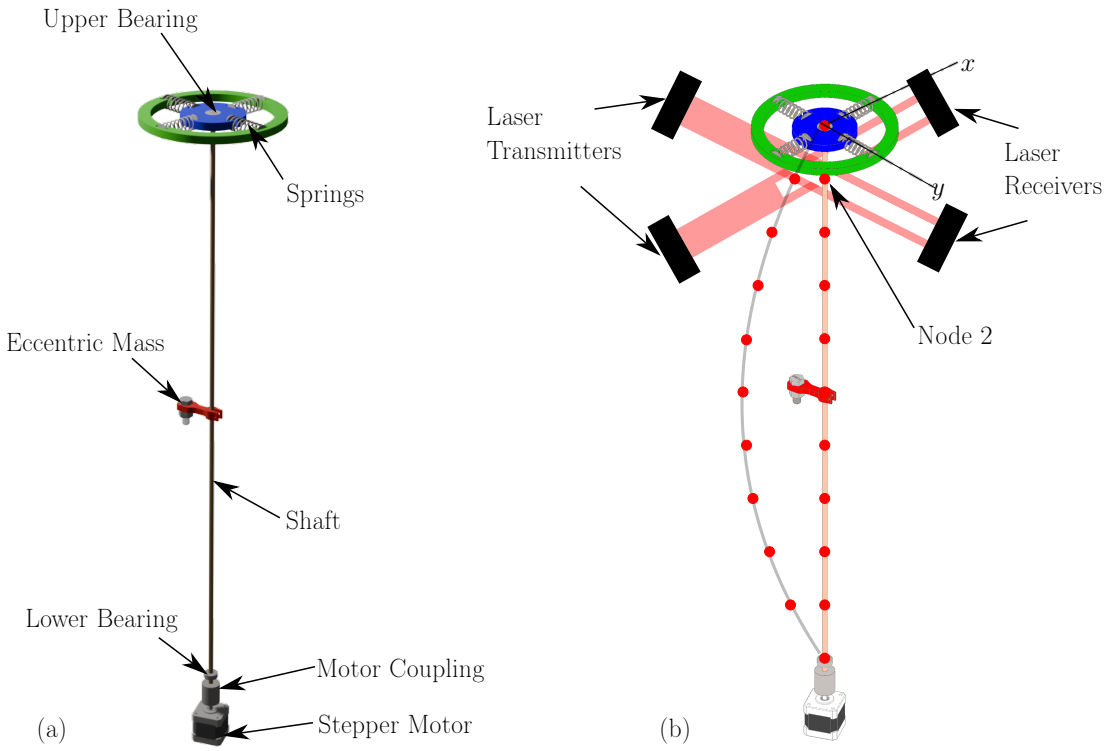

Fig. 3 Schematic of the VARM built at Polytechnique Montréal. (a) Components of the VARM. (b) Laser Sensor mounting on the VARM. The red circles (●) represent nodes that divide the shaft into 10 finite elements.

machine, the actual separation distance of the transmitter and receiver placed along the x-axis is 343 mm, while for those along the y-axis, it is 317 mm. Using a sampling rate of 2 kHz, these instruments are able to capture every significant displacement response of the shaft. The design of this machine and the selection of its various parts are explained in Ref. [31].

3.2 VARM Mathematical Model

Figure 4 illustrates a schematic of the VARM, which includes a uniform shaft of length L, Young's modulus E, radius r, cross-sectional area moment of inertia I, and mass per unit length m. At rest, the shaft lies on the $z-$axis and its motion in time t in the x and y directions is described by $u(z,t)$ and $v(z,t)$, respectively. Excluding the upper and lower bearings, the partial differential equations that describe the rotating motion of the shaft under a rotational speed of Ω and induce transverse vibrations in two perpendicular directions are as follows:

$$m\frac{\partial^2 u(z,t)}{\partial t^2} + c\frac{\partial u(z,t)}{\partial t} + EI\frac{\partial^4 u(z,t)}{\partial z^4} - m\Omega^2 u(z,t) = f_x(z,t), \tag{12}$$

$$m\frac{\partial^2 v(z,t)}{\partial t^2} + c\frac{\partial v(z,t)}{\partial t} + EI\frac{\partial^4 v(z,t)}{\partial z^4} - m\Omega^2 v(z,t) = f_y(z,t), \tag{13}$$

where the external forces $f_x(z,t)$ and $f_y(z,t)$ act on the shaft due to rotational unbalance, and the terms $m\Omega^2 u(z,t)$ and $m\Omega^2 v(z,t)$ correspond to the centrifugal force that stems from the unbalance caused by the shaft's deflection relative to its rotational center. The derivation of equations (12) and (13) was conducted using the principles outlined in Ref. [32] and leveraging the Euler Beam Element theory. However, it is important to mention that the rotational inertia term was omitted due to the shaft's radius being much smaller than its length, specifically $r^2/L^2 \ll 1$. Additionally, the gyroscopic term was disregarded because of the factor $mr^2\Omega/L^2c \ll 1$.

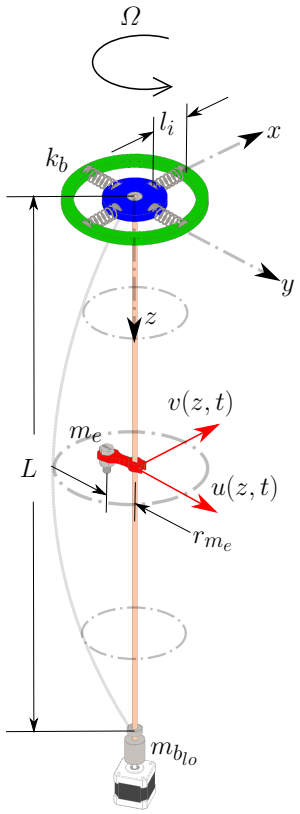

Fig. 4 Schematic representation of the VARM showing different parameters.

The force terms $f_x(z,t)$ and $f_y(z,t)$ are a combination of two components, the first of which arises from the rotating unbalance due to the eccentric mass m_e with a lever arm r_{m_e} positioned at $z = z_{m_e}$, represented by:

$$f_{x1}(z,t) = m_e r_{m_e} \Omega^2 \cos(\Omega t)\delta(z - z_{m_e}), \quad (14)$$
$$f_{y1}(z,t) = m_e r_{m_e} \Omega^2 \sin(\Omega t)\delta(z - z_{m_e}). \quad (15)$$

The second force component consists of a distributed unbalance force arising from the deflection of each element along the shaft, represented by:

$$f_{x2}(z,t) = m(u(z) + u_0(z))\Omega^2 \cos(\Omega t), \quad (16)$$
$$f_{y2}(z,t) = m(v(z) + v_0(z))\Omega^2 \sin(\Omega t), \quad (17)$$

where $u_0(z)$ and $v_0(z)$ represent minor deformations in the shaft when it is stationary, caused by material flaws or mounting imperfections. The shaft experiences damping, characterized by the damping coefficient c. Additional details on this will be provided later.

The bearings at the top and bottom are considered mixed boundary conditions. Each bearing is modeled as a spring-mass-damper system located at each extremity of the shaft. The lower bearing restricts the shaft's movement in both directions, thus it can be represented as a straightforward linear mass-spring-damper system with a very high stiffness coefficient:

$$f_{b_{lo_x}} = -m_{b_{lo}} \frac{\partial^2 u(L,t)}{\partial t^2} - c_{b_{lo}} \frac{\partial u(L,t)}{\partial t} - k u(L,t), \quad (18)$$
$$f_{b_{lo_y}} = -m_{b_{lo}} \frac{\partial^2 v(L,t)}{\partial t^2} - c_{b_{lo}} \frac{\partial v(L,t)}{\partial t} - k v(L,t), \quad (19)$$

where $m_{b_{lo}}$, $c_{b_{lo}}$, and k are the lower bearing mass, damping coefficient, and stiffness coefficient, respectively.

Similarly, the upper bearing can be modeled as a mass-spring-damper system, the mass being that of the bearing and its housing and the damping force being that due to friction and air resistance. Since this force is difficult to measure precisely, we will model it as a viscous damping force with an unknown coefficient affecting both directional movements. This coefficient will have to be determined from data.

We present two models for the upper bearing stiffness force: A Geometric Model, and an Expansion Model which uses a Taylor series expansion. Details are discussed next.

Geometric Model - Geometric Stiffness Force: Figure 5a presents a diagram of the upper bearing. The mass of the bearing housing is $m_{b_{up}}$, and it is attached to four springs arranged perpendicularly, each having an unspecified stiffness denoted by k_b. When the bearing and its housing move from position 1 to position 2, the springs are either stretched or compressed, depending on the movement direction as illustrated in Figure 5b. Each spring generates a force, F_s, following Hooke's law along its axis. This force is described by:

$$F_s = -k_b(l_f - l_i), \quad (20)$$

where l_i is the spring's unstretched length and l_f represents its deformed length.

To determine the overall force produced by the four springs in both the x and y directions, we use a rotation matrix to multiply the force in each spring F_s:

$$\mathbf{R}_i = \begin{bmatrix} \cos(\theta_i) & -\sin(\theta_i) \\ \sin(\theta_i) & \cos(\theta_i) \end{bmatrix}, \; i = 1,2,3,4, \quad (21)$$

with θ_i being assigned one of the four values (0^o, 90^o, 180^o, and 270^o) that represent each spring's orientation. Based on that, the net spring forces along the x and y axes are represented as follows:

$$\begin{bmatrix} F_{T_x} \\ F_{T_y} \end{bmatrix} = \sum_{i=1}^{4} \mathbf{R}_i \begin{bmatrix} F_{is_x} \\ F_{is_y} \end{bmatrix} =$$
$$\begin{bmatrix} -\frac{k_b}{l_i^2} u^3(0,t) + \frac{4k_b}{l_i^2} u(0,t)v^2(0,t) - 2k_b u(0,t) \\ -\frac{k_b}{l_i^2} v^3(0,t) + \frac{4k_b}{l_i^2} v(0,t)u^2(0,t) - 2k_b v(0,t) \end{bmatrix}, \quad (22)$$

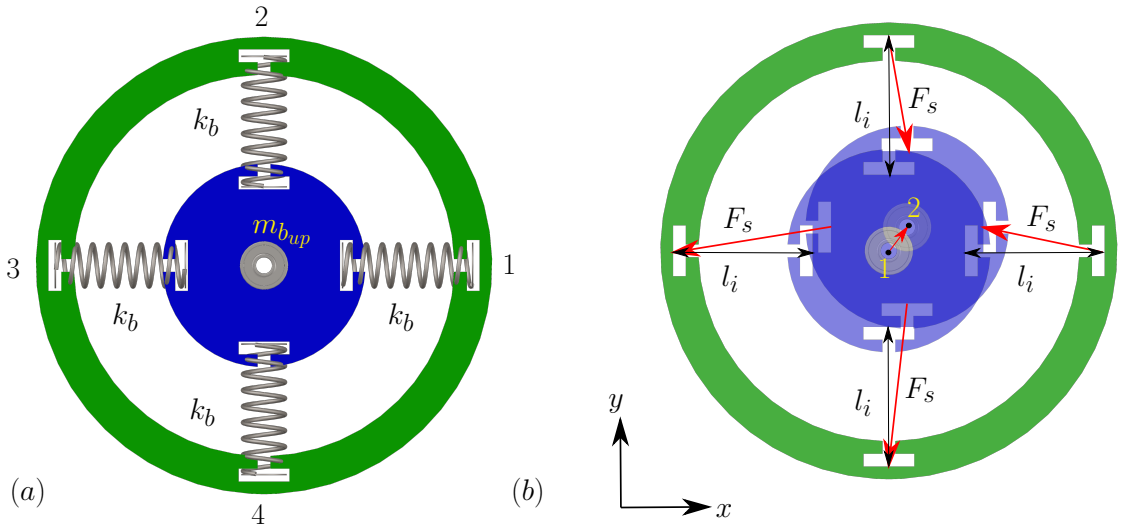

Fig. 5 Compliant bearing attached to the upper end of the shaft. (a) Bearing parameters. (b) Schematic showing spring forces.

where F_{is_x} and F_{is_y} represent the force components produced by spring i along the x and y axes, respectively.

Expansion Model - Taylor Expansion of the Stiffness Force: The model developed in the previous subsection is based on having prior knowledge of both the quantity and arrangement of the springs, which is not always available. Therefore, we have broadened our approach to address scenarios in which the stiffness force function of the upper bearing remains unknown. Acknowledging the inherently nonlinear nature of the stiffness function, we propose the following equations to characterize the stiffness force in the upper bearing:

$$\begin{aligned} F_{T_x} &= -\frac{k_1}{l_i^2}u^3(0,t) - \frac{k_2}{l_i}u^2(0,t) - k_3u(0,t) \\ -k_4\frac{\partial u(0,t)}{\partial z} &- \frac{k_5}{l_i}u(0,t)v(0,t) - k_6(\frac{\partial u(0,t)}{\partial z})^3 \\ &- \frac{k_7}{l_i^2}u(0,t)v^2(0,t), \end{aligned} \tag{23}$$

$$\begin{aligned} F_{T_y} &= -\frac{k_1}{l_i^2}v^3(0,t) - \frac{k_2}{l_i}v^2(0,t) - k_3v(0,t) \\ -k_4\frac{\partial v(0,t)}{\partial z} &- \frac{k_5}{l_i}v(0,t)u(0,t) - k_6(\frac{\partial v(0,t)}{\partial z})^3 \\ &- \frac{k_7}{l_i^2}v(0,t)u^2(0,t). \end{aligned} \tag{24}$$

It is noted that we retained the terms from the explicit model and incorporated additional linear and nonlinear terms that could impact the response. The parameters k_1 through k_7 are variables that must be determined later.

In both models, the upper bearing mass-spring - damper system is represented by:

$$f_{b_{up_x}} = -m_{b_{up}}\frac{\partial^2 u(0,t)}{\partial t^2} - c_{b_{up}}\frac{\partial u(0,t)}{\partial t} - F_{T_x}, \tag{25}$$

$$f_{b_{up_y}} = -m_{b_{up}}\frac{\partial^2 v(0,t)}{\partial t^2} - c_{b_{up}}\frac{\partial v(0,t)}{\partial t} - F_{T_y}, \tag{26}$$

where $c_{b_{up}}$ is the damping coefficient of the upper bearing.

Finally, combining equations (12), (14), (16), (18), (25) in the x direction and equations (13), (15), (17), (19), (26) in the y direction, we derive the complete mathematical model of the VARM as represented by the following two equations:

$$\begin{aligned} &m\frac{\partial^2 u(z,t)}{\partial t^2} + c\frac{\partial u(z,t)}{\partial t} + EI\frac{\partial^4 u(z,t)}{\partial z^4} \\ &-f_{b_{lo_x}}\delta(z-L) - f_{b_{up_x}}\delta(z) - m\Omega^2 u(z,t) \\ &\quad = m_e r_{m_e}\Omega^2\cos(\Omega t)\delta(z-z_{m_e}) \\ &\quad +m(u(z)+u_0(z))\Omega^2\cos(\Omega t), \end{aligned} \tag{27}$$

$$\begin{aligned} &m\frac{\partial^2 v(z,t)}{\partial t^2} + d\frac{\partial v(z,t)}{\partial t} + EI\frac{\partial^4 v(z,t)}{\partial z^4} \\ &-f_{b_{lo_y}}\delta(z-L) - f_{b_{up_y}}\delta(z) - m\Omega^2 v(z,t) \\ &\quad = m_e r_{m_e}\Omega^2\sin(\Omega t)\delta(z-z_{m_e}) \\ &\quad +m(v(z)+v_0(z))\Omega^2\sin(\Omega t). \end{aligned} \tag{28}$$

Equations (27) and (28) serve as the continuous analytical framework of the VARM for both movement directions. To derive a numerical solution, these equations must be discretized, facilitating manipulation through computer-based numerical methods. The Galerkin method is used in a finite element analysis to formulate the weak form of the equations. This finite element model relies

Table 1 List of known parameters of the VARM model.

Parameter	Symbol	Value
Mass per unit length [kg m^{-1}]	m	0.35
Young's Modulus of bronze [GPa]	E	110.3
Shaft radius [m]	r	0.003175
Area moment of inertia [m^4]	I	79.81e-11
Upper bearing mass [kg]	$m_{b_{up}}$	0.056
Unstretched spring length [m]	l_i	0.0508
Lower bearing mass [kg]	$m_{b_{lo}}$	0.176
Lower bearing damping ratio	$\zeta_{b_{lo}}$	0.05
Lower bearing stiffness [N m^{-1}]	k	10^4
Eccentric mass [kg]	m_e	0.0000, 0.0148, 0.0259
Eccentricity [m]	r_{m_e}	0.040
Eccentric mass position [m]	z_{m_e}	0.425
Shaft length [m]	L	0.850
Number of elements	n	10
Mass of one element [kg]	m_{el}	0.0281

on $1D$ beam shape functions, which specify two degrees of freedom at each node located at the ends of each beam element: deflections and the slopes of deflection curves. For further information on this step, the reader is advised to consult Ref. [33]. The discretized version of the equations is presented by:

$$\begin{aligned}
&\begin{bmatrix}\mathbf{M_x} & \mathbf{0}\\ \mathbf{0} & \mathbf{M_y}\end{bmatrix}\begin{Bmatrix}\vec{\ddot{\mathbf{u}}}\\ \vec{\ddot{\mathbf{v}}}\end{Bmatrix}+\begin{bmatrix}\mathbf{C_x} & \mathbf{0}\\ \mathbf{0} & \mathbf{C_y}\end{bmatrix}\begin{Bmatrix}\vec{\dot{\mathbf{u}}}\\ \vec{\dot{\mathbf{v}}}\end{Bmatrix}\\
&+\left[\begin{bmatrix}\mathbf{K_x} & \mathbf{0}\\ \mathbf{0} & \mathbf{K_y}\end{bmatrix}-\Omega^2\begin{bmatrix}\mathbf{M_x} & \mathbf{0}\\ \mathbf{0} & \mathbf{M_y}\end{bmatrix}\right]\begin{Bmatrix}\vec{\mathbf{u}}\\ \vec{\mathbf{v}}\end{Bmatrix}\\
&+\begin{bmatrix}\mathbf{K_{nl1_x}} & \mathbf{0}\\ \mathbf{0} & \mathbf{K_{nl1_y}}\end{bmatrix}\begin{Bmatrix}\vec{\mathbf{u}}^3\\ \vec{\mathbf{v}}^3\end{Bmatrix}\\
&-\begin{bmatrix}\mathbf{K_{nl2_x}} & \mathbf{0}\\ \mathbf{0} & \mathbf{K_{nl2_y}}\end{bmatrix}\begin{Bmatrix}\vec{\mathbf{v}}^2\\ \vec{\mathbf{u}}^2\end{Bmatrix}\begin{Bmatrix}\vec{\mathbf{u}}\\ \vec{\mathbf{v}}\end{Bmatrix}=\begin{Bmatrix}\vec{\mathbf{f_x}}\cos(\Omega t)\\ \vec{\mathbf{f_y}}\sin(\Omega t)\end{Bmatrix}.
\end{aligned}\tag{29}$$

It is important to mention that this equation pertains to the Geometric Model for bearing stiffness, with a comparable method applied to the Expansion Model. In equation (29), the square and cube operations, as well as the vector multiplication in the fourth and fifth terms, are implemented element-wise. The subscripts x and y denote the directions of motion. Consequently, we will define the matrices without indicating the direction, without losing generality. The mass matrix $\mathbf{M}$ represents the mass associated with the shaft, combined with the masses of the bearings and the rotating unbalance. $\mathbf{K}$ represents the linear stiffness matrix including shaft stiffness and linear bearing stiffness coefficients. The matrices $\mathbf{K_{nl1}}$ and $\mathbf{K_{nl2}}$ are primarily zero matrices except the element corresponding to the node where the upper bearing is connected, where the nonlinear coefficient value is included. The vectors $\{\vec{\mathbf{f_x}}\}$ and $\{\vec{\mathbf{f_y}}\}$ specify the forcing term amplitudes due to the eccentric mass and the distributed unbalance force arising from the shaft's initial deflection, respectively. They can be expressed as follows:

$$\begin{Bmatrix}\vec{\mathbf{f_x}}\\ \vec{\mathbf{f_y}}\end{Bmatrix}=\begin{Bmatrix}m_e r_{m_e}\Omega^2\{\vec{\gamma}\}_{z_{m_e}}+m_{el}q_x\{\vec{\mathbf{\Phi_1}}\}\Omega^2\\ m_e r_{m_e}\Omega^2\{\vec{\gamma}\}_{z_{m_e}}+m_{el}q_y\{\vec{\mathbf{\Phi_1}}\}\Omega^2\end{Bmatrix}.\tag{30}$$

In this context, $\{\vec{\gamma}\}_{z_{m_e}}$ is a vector that consists predominantly of zeros, except it has a value of 1 at the node linked to the distance z_{m_e}. The second term can be perceived as a distributed eccentric force, where each element is an eccentric mass of m_{el}. The eccentricity can be determined by considering the beam's initial bending and the deflection caused by rotational movement, which can be expressed as $q_x\{\vec{\mathbf{\Phi_1}}\}$. The beam's dynamics are mainly influenced by its first mode; hence, we chose to express the beam's deflection using its primary eigenvector, $\{\vec{\mathbf{\Phi_1}}\}$, which is derived from solving the system's eigenvalue problem through its mass and stiffness matrices. This eigenvector is scaled with an unidentified factor q_x, which needs to be estimated from experimental data. A similar approach is applied for representation in the y-direction.

To conclude, the matrix $\mathbf{C}$ serves as the damping matrix, incorporating both structural damping and damping derived from bearing models. The structural damping component $\mathbf{C_s}$ is expressed using Rayleigh damping, specifically by considering only the mass-proportional term as shown below:

$$\mathbf{C_s}=\alpha_d\mathbf{M}.\tag{31}$$

Here, the structural damping coefficient ζ_s can be defined as:

$$\zeta_s = \frac{1}{2}\frac{\alpha_d}{\omega_1}, \tag{32}$$

with ω_1 representing the system's first modal frequency.

Table 1 presents all the known parameters of the general VARM model, which includes both measured and computed values. An arbitrarily large value was selected for the lower bearing stiffness, along with a comparatively elevated damping ratio, aligned with the damping properties of rubber [34], since a rubber bushing was placed between the shaft and the lower bearing. This ensures that the node linked to the lower bearing consistently has a displacement of zero in our calculations due to the high stiffness and/or high damping ratio.

4 Results

This section verifies the effectiveness of the developed method by applying it to the Geometric and Expansion Models.

4.1 Geometric Model

White-Box Model: In the Geometric Model, we identify $n_p = 5$ difficult-to-measure parameters and enumerate them in Table 2.

For a given rotational speed, the Latin hypercube generated $n_s = 1000$ scenarios. The HMH solver was used to solve these n_s scenarios to obtain their steady state limit cycles. The time series of two steady state cycles of all DOFs of the system were stored in the $\mathbf{U}(z,t)$ and $\mathbf{V}(z,t)$ matrices for the x- and y-direction displacements respectively. With 10 elements along the shaft, there are 11 nodes, each possessing 4 DOFs, thus resulting in $n_{DOF} = 44$. Figure 3b illustrates these nodes depicted as red circles positioned along the shaft. Each rotational speed corresponds to a unique time duration that covers 2 full cycles, represented by $T_{2cyc} = 120/\Omega$ s, where Ω is the VARM's rotational speed in RPM. The number of time steps, n_t, for 2 cycles is influenced by the rotational speed, typically calculated as $n_t = T_{2cyc}/dt$, with $dt = 5e-4$ s being the duration of one time step.

To choose a sufficient number of reduced-order modes to fully represent the VARM displacement, the first few normalized singular values were extracted. We observed that the ratio of the second singular value to the first is 0.0012, this means that the data can be effectively represented by the first reduced-order mode alone, with additional modes having an insignificant contribution, i.e. $m_d = 1$. This is due to the high correlation within the dataset, as variations in parameter values across scenarios only influence the response amplitude.

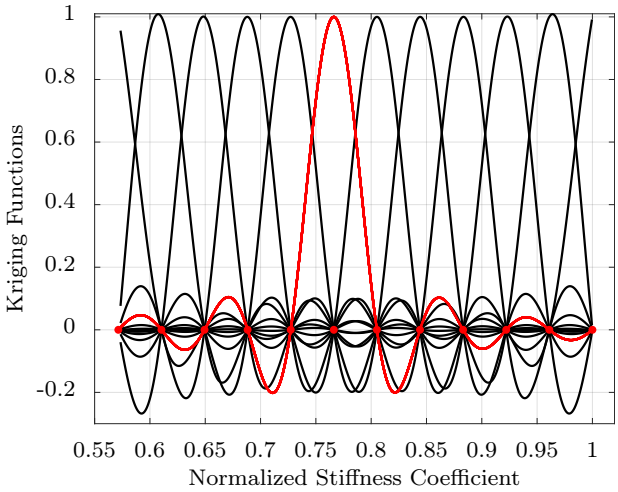

Fig. 6 Globally defined Kriging basis functions used to interpolate the response of the system in terms of the normalized stiffness coefficient. The limits of the non-dimensional domain were derived by normalizing the range in Table 2 with its maximum value. Similar functions are used to interpolate the response in terms of the other parameters. The red circles (●) represent control points. The function in red represents the form of a single Kriging function defined globally on the parameter domain.

Applying equation (6) presented in Section 2.1 to the Geometric Model case with the parameters defined in Table 2, the matrix $\mathcal{U}$ can be represented as a function of the five specific parameters according to the sPGD formulation as follows:

$$\mathcal{U}(k_b, \zeta_s, \zeta_{b_{up}}, q_x, q_y) = \sum_{k=1}^{M} F_1^k(k_b) F_2^k(\zeta_s) F_3^k(\zeta_{b_{up}}) F_4^k(q_x) F_5^k(q_y). \tag{33}$$

where the interpolation functions chosen are the Kriging functions shown in Figure 6. The advantages of using such functions are explained in Ref. [30]. In general, using between 8 and 12 control points provided a satisfactory approximation while preventing over-fitting.

To evaluate the outcomes of the proposed method, it is crucial to initially confirm that the sPGD library yields accurate approximations of the system's response for a random set of parameters. Figure 7 illustrates the orbital motion of the VARM's second node, computed for a random set of parameters via the HMH solver and the sPGD library. The figure demonstrates a strong agreement between the two approaches, indicating that the sPGD is a dependable method for use in the optimization process.

Table 2 List of unknown parameters of the VARM corresponding to the Geometric Model.

Parameter	Symbol	Expected range
Spring stiffness $[\mathrm{N\,m^{-1}}]$	k_b	2000 - 3500
Structural damping ratio	ζ_s	0.01 - 0.05
Upper bearing damping ratio	$\zeta_{b_{up}}$	0.00 - 0.05
Force coefficient (x-axis)	q_x	0.001 - 0.01
Force coefficient (y-axis)	q_y	0.001 - 0.01

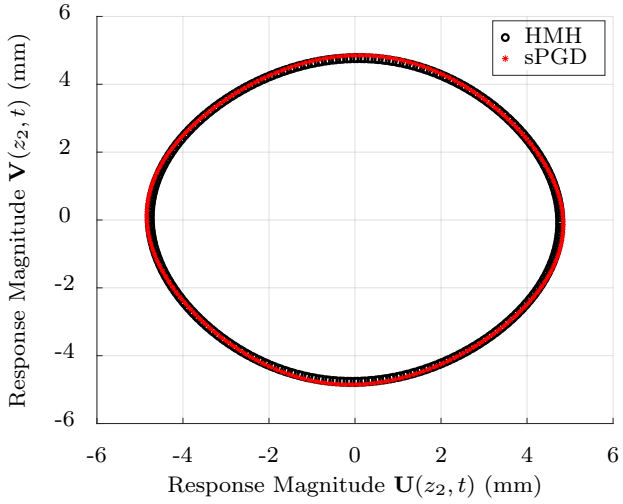

Fig. 7 Orbital motion of the second node of the VARM calculated using the HMH solver and sPGD for the parameters: $k_b = 2750\ \mathrm{N\,m^{-1}}$, $q_x = 0.01$, $q_y = 0.01$, $\zeta_s = 0.02$, $\zeta_{b_{up}} = 0.02$.

Table 3 The values of the eccentric mass used for each range of rotational speed during the experiments.

Rotational Speed Range [RPM]	Eccentric Mass [g]
350 - 650	25.9
550 - 850	14.8
800 - 1000	0.0

Black-Box Model: The VARM system's sensors collect data, which is then processed using a LabView program and analyzed with MATLAB scripts. During the experiments, the motor maintained a constant rotational speed, and the resulting steady-state displacement of the second node was recorded as time series data in both the x and y directions with a time step of $5e-4$ s (a sampling frequency of 2 kHz). Figure 8 displays an example of the collected data. To ensure that the unbalance force acting on the shaft exceeds the preload requirements of the lower bearing without causing machine damage, an appropriate eccentric mass was selected for each speed range through experimental observations, as detailed in Table 3. Data were collected for rotational speeds with 50 RPM increments.

Grey-box Model: At this point, we address the earlier specified optimization problem using the LM optimization method. Given that the bearing stiffness is determined by geometric factors, we omit the sparsity-promoting term, hence $\lambda = 0$, and only the $\mathcal{L}_2$ norm is minimized. In each optimization process, conducting $\tau = 50$ trials proved sufficient to achieve satisfactory outcomes, and the procedure was executed 1000 times within the Monte Carlo framework, with the final result reflecting the average from these 1000 procedures.

Figure 9 illustrates the parameter values as a function of rotational speed and the eccentric mass attached to the shaft. It is observed that the bearing stiffness k_b, structural damping ratio ζ_s, and the bearing damping ratio $\zeta_{b_{up}}$ maintain consistent values, irrespective of changes in the rotational speed or eccentric mass. This consistency emerges because these values signify physical properties expected to remain steady during operation. In contrast, q_x and q_y vary with the eccentric mass and increase as the rotational speed rises. These parameters are correction factors intended to account for shaft bending not otherwise physically modeled. Their variations are characteristic of a centrifugal pull; examining a 1 DOF static form of the equation of motion in the x direction yields:

$$\hat{k}\phi(q_x - q_0) = \Omega^2(m_{el}q_x\phi + m_e r_{m_e}), \tag{34}$$

where q_0 is the initial bending in the shaft, $\hat{k}$ is the stiffness of 1 DOF of the shaft, and ϕ is a 1 DOF version of the first eigenvector of the VARM. This equation rearranges to:

$$q_x = \frac{\hat{k}\phi q_0 + \Omega^2 m_e r_{m_e}}{\hat{k}\phi - \Omega^2 m_{el}\phi}, \tag{35}$$

displaying the relationship between q_x and Ω. Two scenarios arise: with an eccentric mass, $m_e >> m_{el}$, the equation simplifies to:

$$q_x = \frac{\hat{k}\phi q_0 + \Omega^2 m_e r_{m_e}}{\hat{k}\phi}, \tag{36}$$

without an eccentric mass, where $m_e = 0$, the equation becomes:

$$q_x = \frac{\hat{k}\phi q_0}{\hat{k}\phi - \Omega^2 m_{el}\phi}. \tag{37}$$

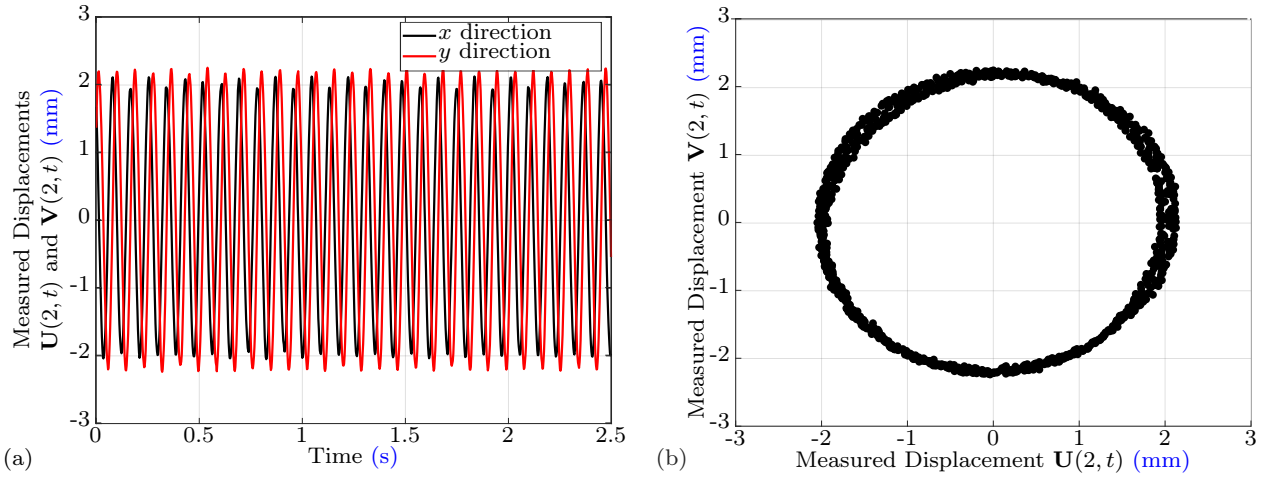

Fig. 8 Example of the measured displacement of node 2 on the shaft in the x and y directions. Case corresponds to an eccentric mass of 14.8 g and a rotational speed of 700 RPM. (a) Time series. (b) Orbital motion.

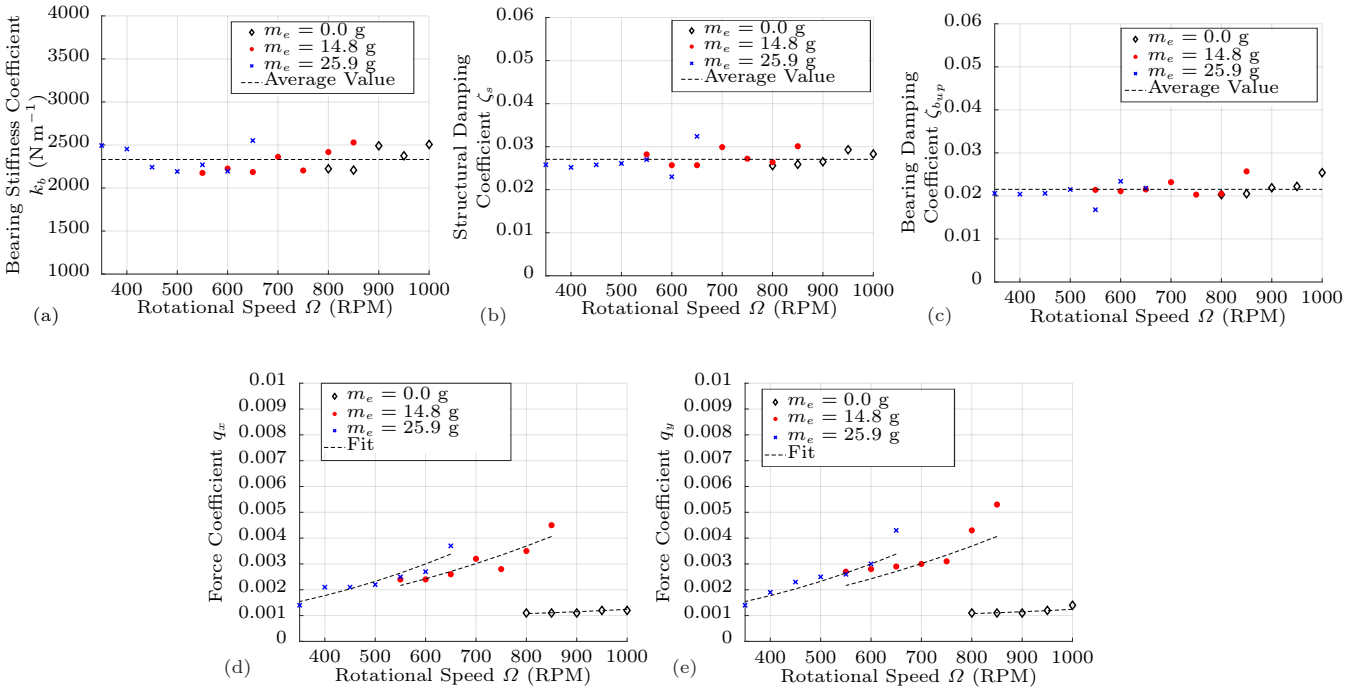

Fig. 9 Optimal values of VARM parameters. (a) Bearing Stiffness Coefficient $k_b = 2331.5$ (N m^{-1}). (b) Structural Damping Coefficient $\zeta_s = 0.0271$. (c) Bearing Damping Coefficient $\zeta_{b_{up}} = 0.0215$. (d) Force Coefficient q_x. (e) Force Coefficient q_y.

Equations (36) and (37) are explicitly used to find the optimal fitting line for q_x and q_y graphs relative to Ω. Figure 9 shows that these theoretical relations align well with the empirical results, thus confirming their reliability.

Figure 10 depicts the orbital displacement of the second node of the shaft as it relates to the rotational speed and eccentric mass. The black dots indicate data gathered from the VARM, while the blue line illustrates the calculated response derived from the optimized parameters calculated using the LM algorithm. The figure demonstrates that the calculated response agrees well with the measured data across all values of rotational speed and eccentric masses, confirming that the optimal parameters accurately represent the system's behavior.

Exploring the behavior of the LM optimization technique, an optimization process involves τ randomly initialized trials, each starting with a different random parameter set. The algorithm then selects the trial that minimizes the loss function to determine the solution for that optimization process. Figure 11 illustrates the progression of the loss function's value across 50 trials, highlighting in red the trial that minimizes the loss

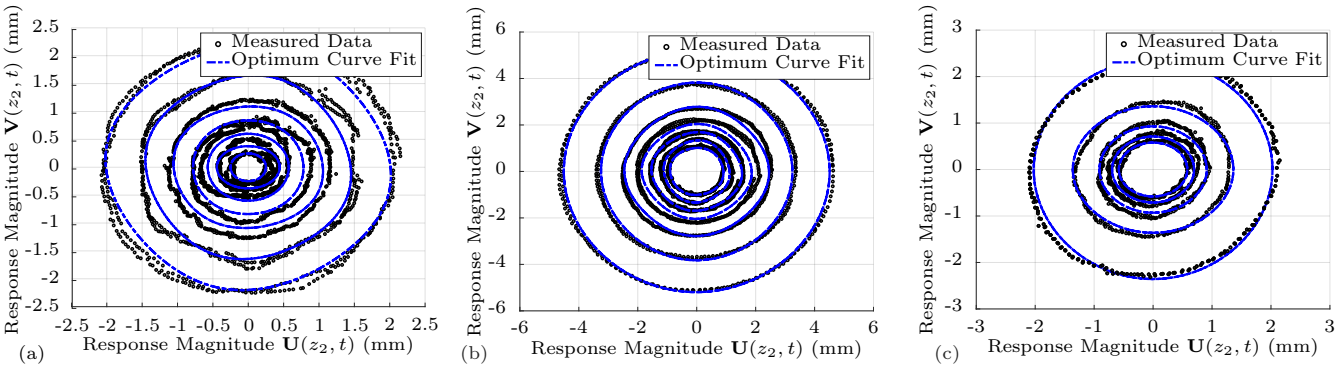

Fig. 10 Optimal orbital displacement of the second node of the shaft vs. measured data for various values of eccentric mass and rotational speeds. (a) $m_e = 25.9$ g, $\Omega = [350, 650]$ RPM. (b) $m_e = 14.8$ g, $\Omega = [550, 850]$ RPM. (c) $m_e = 0$ g, $\Omega = [800, 1000]$ RPM.

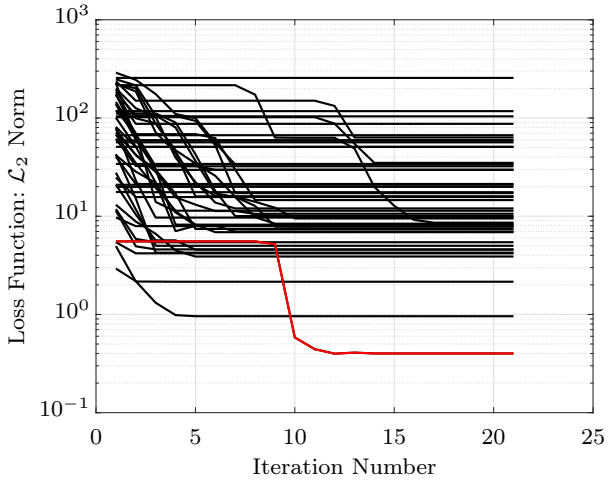

Fig. 11 Loss function evolution for 50 trials of one optimization process when $m_e = 14.8$ g and $\Omega = 700$ RPM. The red line represents the selected trial that minimizes the loss function.

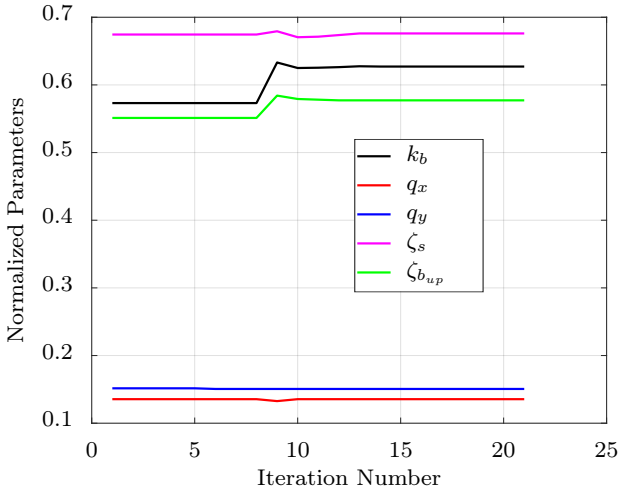

Fig. 12 Parameter convergence for the selected trial that minimizes the loss function of one optimization process when $m_e = 14.8$ g and $\Omega = 700$ RPM.

function. This corresponds to the case where $m_e = 14.8$ g and $\Omega = 700$ RPM.

Figure 12 illustrates the evolution of the 5 parameters toward their chosen optimal value in the case highlighted above. It is important to note that the parameter values depicted in the figure are normalized. Observing the data, we find that the parameters q_x and q_y have less impact on the system's response compared to the other parameters.

Eccentric Mass as an Additional Parameter: In our model, the eccentric mass was easily identified using a digital scale. However, in this section, we treat the eccentric mass as unknown, incorporating it as a sixth parameter in our system for estimation. The corresponding results are presented in Figure 13. We observe that the eccentric mass exhibits a consistent value irrespective of the rotational speed, although it is slightly underestimated in the initial two cases. In the first case, the actual value

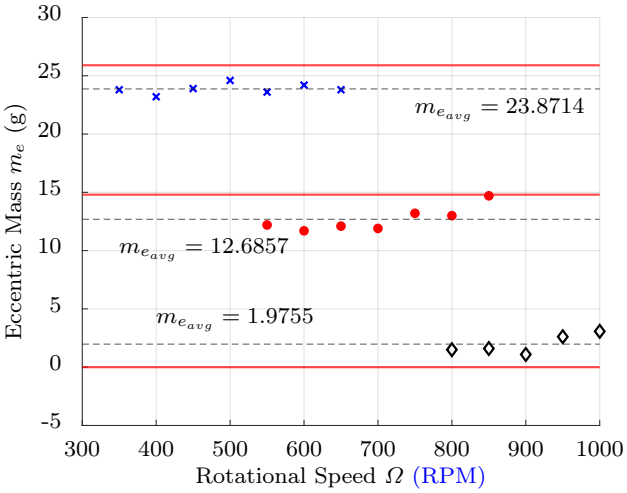

Fig. 13 Optimized Value of the Eccentric Mass. The red line represents the true value, and the dashed line represents the average of the predicted values.

is 25.9 g, while our method predicts 23.9 g, resulting in a 7.7% error. In the second case, the true value is 14.8 g with our estimation at 12.7 g, leading to a 14.2% error. Notably, in the third case, there was no eccentric mass, yet the predicted value was 1.9 g. This can be attributed to the domain on which the sPGD was trained, which spans $[0, 10]$ g. Since 0 is an edge value, the sPGD interpolation struggles to precisely reach it. Nonetheless, these discrepancies arise because when the LM algorithm attempts to determine values for six parameters concurrently to minimize a single loss function, some compromise is inevitable to achieve an overall response that most closely aligns with the data. To provide a numerical explanation, we observed that in the Geometric Model, when the eccentric mass values are known, the predicted bearing stiffness came to 2331.5 $\mathrm{N\,m^{-1}}$. Conversely, in the model with predicted masses, the stiffness predicted was 2443.6 $\mathrm{N\,m^{-1}}$. This indicates that underestimating the eccentric mass led to an overestimation of the bearing stiffness as a compensatory measure to minimize the loss function.

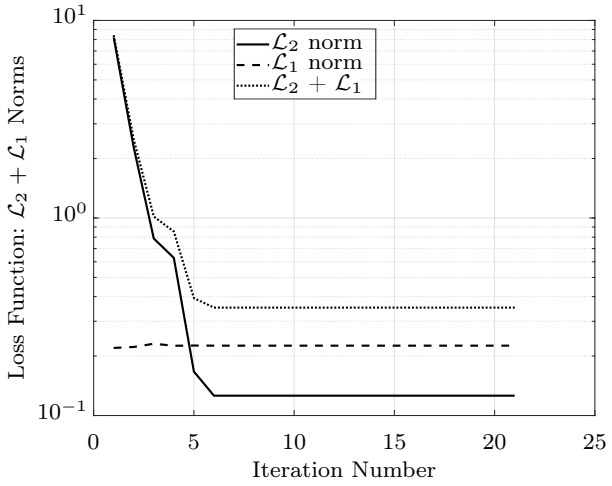

Fig. 14 Loss function evolution for the selected trial of one optimization process when $m_e = 14.8$ g and $\Omega = 700$ RPM.

4.2 Expansion Model

The Expansion Model involves determining $n_p = 9$ parameters, specifically k_1 through k_7 along with q_x and q_y. The values for ζ_s and $\zeta_{b_{up}}$ are sourced from predictions of the Geometric Model. Given the model's complexity, we employed Latin hypercube sampling to create $n_s = 2700$ scenarios. To accommodate the increased parameter count, the sPGD algorithm required additional control points, with 15 to 20 being adequate.

We employed the same optimization strategy to estimate these parameters but with a minor adjustment that involved incorporating a sparsity promoting term $\lambda = 0.1$ into the loss function as detailed in equations (9,10,11) in the methodology. λ is a hyper-parameter that was chosen to be sufficiently large to ensure that $\mathcal{L}_1$ contributed a meaningful sparsity component, aiding in assessing parameter significance, while remaining small enough to preserve the significance of $\mathcal{L}_2$. Figure 14 illustrates the original least squares error loss function, the added sparsity loss function, and their combined effect. Although the inclusion of the sparsity term raises the loss function's final value, it ensures that the total sum of predicted parameters is minimized, aiding in identifying which parameters significantly influence the system's response. Additionally, the $\mathcal{L}_1$ norm tends to stay relatively stable throughout the optimization process. This is due to the fact that the algorithm selects the trial with the least error in each optimization procedure. In these successful trials, the initial parameter values were generally close to their eventual converged values, leading to only slight fluctuations during optimization, as depicted in Figure 12. By definition, the $\mathcal{L}_1$ norm mirrors the behavior of the parameter values, as it calculates their average multiplied by the hyper-parameter λ, thus maintaining a nearly steady value. On the other hand, the $\mathcal{L}_2$ norm depends on the system's response to the parameter set derived from the sPGD surrogate model, making it more prone to slight changes in parameter values.

The remaining hyper-parameters that were not specifically mentioned here were the same as those used for the Geometric Model. Same data sets were used as well.

Table 4 displays the optimum normalized values for the bearing stiffness parameters $k_1 - k_7$. These values represent the average of values obtained for the same ranges of eccentric mass and rotation speeds used in the Geometric Model. The parameters k_2, k_5, and k_7 are distinctly smaller but not negligible when assessed purely on a mathematical basis using the gathered data. However, incorporating physical considerations, a stronger case can be made for their exclusion. This further emphasizes the benefits of the grey-box framework. The terms associated with k_2 and k_5 have no physical relevance in the model and can thus be omitted. In contrast, k_7 depicts the coupling between the shaft's motion along the x and y axes. Yet, as demonstrated in the upcoming section, omitting k_7 has a negligible effect on the overall results, allowing us to treat the shaft's motion as uncoupled. Nevertheless, k_7 converged to a negative value leading to a positive coupling term in eqs. (23) and (24), and this conforms with the Geometric model in eq. (22) Another observation is that the two terms related to the displacement's slope (k_4 and k_6), which were overlooked in the Geometric Model, appear to have a significant effect. Lastly, as

Table 4 Optimized Values of the Bearing Stiffness Parameters in the Expansion Model

Parameter	Normalized Value	Actual Value
k_1	0.732	2562.7 [N m^{-1}]
k_2	−0.071	−70.9 [N m^{-1}]
k_3	0.775	5428.5 [N m^{-1}]
k_4	0.341	341.1 [N]
k_5	−0.061	60.9 [N m^{-1}]
k_6	0.293	293.0 [N]
k_7	−0.045	−627.7 [N m^{-1}]

anticipated from the geometry, the actual value of k_1 is approximately half the value of k_3, a relationship that was explicitly depicted in the Geometric Model.

4.3 Combining the Geometric and Expansion Models towards the Hybrid Twin

Analyzing the parameter values using the Expansion Model provided more clarity on the overall depiction of the bearing stiffness force. We found that the coupled term in the Geometric Model is not substantial. However, two additional crucial terms concerning shaft bending have more influence on the accuracy of the entire function. Consequently, we chose to express the stiffness force in the upper bearing as follows:

$$F_{T_x} = -\frac{k_b}{l_i^2}u^3(0,t) - 2k_b u(0,t) - k_w\frac{\partial u(0,t)}{\partial z} - k_z(\frac{\partial u(0,t)}{\partial z})^3, \tag{38}$$

$$F_{T_y} = -\frac{k_b}{l_i^2}v^3(0,t) - 2k_b v(0,t) - k_w\frac{\partial v(0,t)}{\partial z} - k_z(\frac{\partial v(0,t)}{\partial z})^3, \tag{39}$$

These equations include three unknown parameters: k_b, k_w, and k_z, along with the two damping parameters $\zeta_{b_{up}}$ and ζ_s, and the two force coefficients q_x and q_y. We recalculated the values of these seven parameters in our final model. The values of q_x and q_y exhibit a pattern similar to that depicted in Figure 9, while the remaining values are documented in Table 5. It is important to mention that in this instance, the parameters were determined without incorporating the sparsity loss term, meaning $\lambda = 0$, because our findings suggest that all parameters hold significance.

Figure 15 illustrates that despite eliminating the extra terms, the data continues to align closely with the simulated response. This implies that the final model indeed acts as a hybrid twin of the physical machine,

Table 5 Optimized Values of the Bearing Final Model Parameters

Parameter	Optimized Value
k_b [N m^{-1}]	2411.3
k_w [N]	324.2
k_z [N]	301.1
ζ_s	0.024
$\zeta_{b_{up}}$	0.016

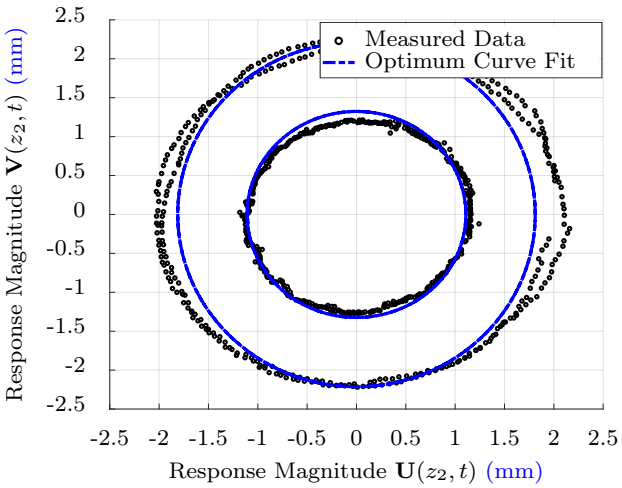

Fig. 15 Orbital displacement of the second node of the shaft. The large circle represents the case where $m_e = 14.8$ g and $\Omega = 700$ RPM, and the small circle represents the case where $m_e = 25.9$ g and $\Omega = 550$ RPM.

capable of predicting its behavior across different scenarios. The model's validity is further confirmed by testing it with a separate dataset not involved in the parameter optimization. In this instance, an eccentric mass of three different values was used. The findings are presented in Figure 16 where the empirical data aligns with the simulated response for eccentric mass values not used during the construction of the hybrid twin. It is crucial to note that the parameters q_x and q_y were adjusted based on the mass values, as they depend on the mass values as seen in the results.

The method proved to be efficient in producing the anticipated results, but it still has limitations. First, it should be noted that when generating the parameter data set used to build the surrogate model via sPGD, the number of scenarios n_s is selectable, though the Latin Hypercube algorithm randomly distributes the parameter values of these scenarios throughout the parameter domain to ensure comprehensive coverage. Also, as sPGD is a form of interpolation, it cannot handle the situation where the true parameter values are outside the expected range. Therefore, initial estimates of the parameter ranges were established through

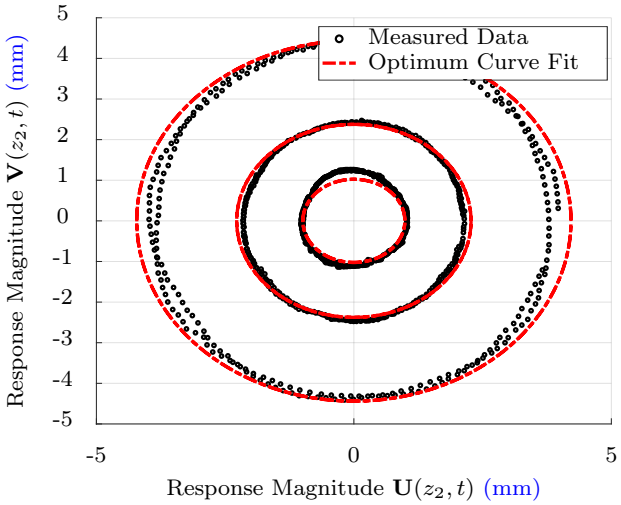

Fig. 16 Orbital displacement of the second node of the shaft. The large circle represents the case where $m_e = 7.6$ g and $\Omega = 900$ RPM, the medium circle represents the case where $m_e = 19.5$ g and $\Omega = 700$ RPM, and the small circle is where $m_e = 36.0$ g and $\Omega = 450$ RPM.

an understanding of the system components and subsequently adjusted by evaluating the identified parameters. It was noted that if any parameters converged to values near the extremities of the predetermined range, it would suggest a need for revising these limits. Another limitation in the system is that although numerous complexities were incorporated during development, the system ultimately displayed a monomodal response. Further tests should be performed in the future with excitations giving rise to a richer modal response.

5 Conclusion and Future Work

In conclusion, this paper introduced an innovative method that integrates established numerical techniques to form a hybrid twin of a VARM subjected to nonlinear bearing forces, rotational unbalance, and varying loading amplitudes and rotational speeds. This hybrid twin relies on the physical principles governing the VARM, which are modeled by partial differential equations comprising some unknown parameters determined through data assimilation from an experimental VARM setup. The findings indicate that when the bearing model is clearly defined, the method reliably predicts various parameters in accordance with physical principles and intuition. In cases where the bearing model is not clearly established, a provisional model was proposed, allowing the method to determine which terms meaningfully affect the machine's behavior by optimizing the parameter values.

In future work, the approach may be expanded to tackle increasingly intricate systems. Vertical-axis hydraulic turbines, like Francis, Kaplan, and propeller turbines, exhibit numerous resemblances to our VARM. These similarities include a flexible rotating shaft supported by bearings at both ends, which apply unknown nonlinear forces, the lateral vibrations induced by whirling and rotational unbalance, as well as the nonlinear dynamic behavior as a whole. However, the hydraulic turbine model not only incorporates dynamic vibrations but also complex fluid-structure interactions due to water flow. Nevertheless, a block method can be employed where each subsystem is independently modeled and solved with its own PDE. The output from one block serves as the input for the next, aiding in the analysis via the proposed methods. Unbalanced mass effects may originate from swirling cavitation, generator imbalance, or irregular water flow caused by blockages in the guide veins. Additionally, typical hydraulic turbine configurations use tilted-pad journal bearings. Literature indicates that the forces exerted by these bearings are described by equations with undetermined coefficients, which can be analyzed using a method akin to the one outlined in this paper.

The method itself can be further enhanced to study the transient regime, as our analysis was limited to the steady-state response. This is important in the application of hydraulic turbines as their operation involves starts and stops that need to be analyzed. There remains potential to explore alternative optimization techniques that could anticipate parameter variations during operation, thereby identifying potential faults. Additionally, various scenarios could be explored by introducing varied loads or using different types of bearings.

Author Contributions

Sima Rishmawi: Writing - original draft, Validation, Software, Resources, Methodology, Formal analysis, Conceptualization, Data curation, Investigation. **Ludivine Moyne**: Building the experimental rig, Carrying out experiments, Data collection. **Souheil Serroud**: Building the experimental rig. **Sebastian Rodriguez**: Writing - review and editing, Software, Methodology. **Francisco Chinesta**: Writing - review and editing, Conceptualization of the study. **Oguzhan Tuysuz**: Writing - review and editing, Supervision. **Frédérick P. Gosselin**: Writing - review and editing, Project Administration, Conceptualization of the study, Funding acquisition.

Conflict of interest

The authors declare that they have no known competing financial interests or personal relationships that could have appeared to influence the work reported in this paper.

Acknowledgments and Funding

The authors would like to acknowledge the technical and financial support of Hydro-Québec and Maya HTT, and the financial support of NSERC Alliance [Grant ALLRP 556353 - 20], InovÉÉ, IVADO [PhD Excellence Scholarship], and Mitacs [Globalink Research Award].

Data Availability

The datasets generated or analyzed during this study are available from the corresponding author upon reasonable request.

Ethical Approval

The authors declare that they comply with ethical standards.

References

1. D. J. Wagg, K. Worden, R. J. Barthorpe, and P. Gardner, "Digital twins: State-of-the-art and future directions for modeling and simulation in engineering dynamics applications," *ASCE-ASME Journal of Risk and Uncertainty in Engineering Systems, Part B: Mechanical Engineering*, vol. 6, March 2020.
2. S. L. Brunton, J. L. Proctor, and J. N. Kutz, "Discovering governing equations from data by sparse identification of nonlinear dynamical systems," in *Proceedings of the National Academy of Sciences of the United States of America*, vol. 113, March 2016.
3. F. Chinesta, E. G. Cueto, E. Abisset-Chavanne, J. L. Duval, and F. A. Khaldi, "Virtual, digital and hybrid twins: A new paradigm in data-based engineering and engineered data," *Archives of Computational Methods in Engineering*, 2019.
4. Y. Ishida and T. Yamamoto, *Linear and Nonlinear Rotordynamics*. Wiley-VCH, 2012.
5. M. I. Friswell, J. E. T. Penny, S. D. Garvey, and A. W. Lees, *Dynamics of Rotating Machines*. Cambridge University Press, 2010.
6. R. Tiwarti, "A brief history of rotor dynamics and recent trends," in *51st Congress of Indian Society of Theoretical and Applied Mechanics (ISTAM) 2006*, (Vishakhapatanam, India), December 2006 2006.
7. M. Nasselqvist, R. Gustavsson, and J.-O. Aidanpaa, "Experimental and numerical simulation of unbalance response in vertical test rig with rilting-pad bearings," *International Journal of Rotating Machinery*, vol. 2014, January 2014.
8. W. J. Chen and E. J. Gunter, *Introduction to Dynamics of Rotor Bearing Systems*. Eigen Technologies, 2007.
9. R. Turaga, A. S. Sekhar, and B. C. Majumdar, "Comparison betwee linear and nonlinear transient analysis techniques to find the stability of a rigid rotor," *Journal of Tribology*, vol. 121, pp. 198–201, January 1999.
10. R. K. Gustavsson, M. L. Lundstrom, and J.-O. Aidanpaa, "Determination of journal bearing stiffness and damping at hydropower generators using strain gauges," in *Proceedings of ASME Power Conference 2005*, (Chicago, Illinois), April 2005.
11. T. W. Diamond, P. N. Sheth, P. E. Allaire, and M. He, "Identification methods and test results for tilting pad and fixed geometry journal bearing dynamic coefficients - a review," *Shock and Vibration*, vol. 16, pp. 13–43, 2009.
12. T. Dimond, A. Younan, and P. Allaire, "A review of tilting pad bearing theory," *International Journal of Rotating Machinery*, vol. 2011, 01 2011.
13. RSR, "Rotordynamics-seal research: Rappid™ rotordynamics software suite."
14. M. Shi, D. Wang, and J. Zhang, "Nonlinear dynamic analysis of a vertical rotor-bearing system," *Journal of Mechanical Science and Technology*, vol. 27, pp. 9–19, August 2012.
15. C. Ghnatios, F. Masson, A. Huerta, A. Leygue, E. Cueto, and F. Chinesta, "Proper generalized decomposition based dynamic data-driven control of thermal processes," *Computer Methods in Applied Mechanics and Engineering*, vol. 213-216, pp. 29–41, March 2012.
16. F. Chinesta, A. Ammar, and E. Cueto, "Recent advances and new challenges in the use of the proper generalized decomposition for solving multidimensional models. archives of computational methods in engineering," *Archives of Computational Methods in Engineering*, vol. 17, 2010.
17. F. Chinesta and E. Cueto, *PGD-Based Modeling of Materials, Structures and Processes*. Springer, 01 2014.
18. A. Ammar, B. Mokdad, F. Chinesta, and R. Keunings, "A new family of solvers for some classes of multidimensional partial differential equations encountered in kinetic theory modeling of complex fluids," *Journal of Non-Newtonian Fluid Mechanics*, vol. 139, pp. 153–176, July 2006.
19. S. Rodriguez, E. Monteiro, N. Mechbal, M. Rebillat, and F. Chinesta, "Hybrid twin of rtm process at the scarce data limit," *International Journal of Material Forming*, vol. 16, no. 4, p. 40, 2023.
20. R. Ibáñez, E. Abisset-Chavanne, A. Ammar, D. González, E. Cueto, A. Huerta, J. L. Duval, F. Chinesta, *et al.*, "A multidimensional data-driven sparse identification technique: the sparse proper generalized decomposition," *Complexity*, vol. 2018, 2018.
21. A. Sancarlos, V. Champaney, J.-L. Duval, E. Cueto, and F. Chinesta, "Pgd-based advanced nonlinear multiparametric regressions for constructing metamodels at the scarce-data limit," 2021.
22. S. Rishmawi, S. Rodriguez, F. Chinesta, and F. P. Gosselin, "Harmonic-modal hybrid frequency approach for parameterized non-linear dynamics," *Computers and Structures*, vol. 301, p. 107461, 2024.
23. C. Germoso, J. L. Duval, and F. Chinesta, "Harmonic-modal hybrid reduced order model for the efficient integration of non-linear soil dynamics," *Applied Sciences (Switzerland)*, vol. 10, September 2020.
24. D. Knight, "Data driven design optimization methodology, a dynamic data driven application system," in *Proceedings of the 2003 International Conference on Computational Science*, pp. 329–336, June 2003.

25. H. P. Gavin, "The levenberg-marquardt algorithm for nonlinear least squares curve-fitting problems," technical report, Department of Civil and environmental Engineering, Duke University, Durham, NC, 2020. accessed: March 15, 2022.
26. T. M. Cameron and J. H. Griffin, "An alternating frequency/time domain method for calculating the steady-state response of nonlinear dynamic systems," *Journal of Applied Mechanics*, vol. 56, March 1989.
27. G. Quaranta, C. A. Martin, R. Ibanez, J. L. Duval, E. Cueto, and F. Chinesta, "From linear to nonlinear pgd-based parametric structural dynamics," *Comptes Rendus - Mecanique*, vol. 347, pp. 445–454, February 2019.
28. K. Karhunen, "Zur spektraltheorie stochastischer prozesse," *Ann. Acad. Sci. Fennicae, AI*, vol. 34, 1946.
29. M. Loeve, "Fonctions aléatoires du second ordre," *Lévy, Processus Stochastiques et Mouvement Brownien, Gauthier-Villars, Paris*, 1948.
30. G. E. Fasshauer, *Meshfree Approximation Methods with Matlab*. World Scientific, 2007.
31. S. Serroud, "Design of a vertical axis rotating machine for the development of a digital twin," master's thesis, École Polytechnique de Montréal, Montréal, QC, Canada, 2023.
32. M. L. Adams, *Rotating Machinery Vibration: From Analysis to Troubleshooting*. Boca Raton, FL: CRC Press, second ed., 2010.
33. D. S. Burnett, *Finite element analysis: From concepts to applications*. Addison-Wesley, 1988.
34. "Structural damping properties of mechanical systems." `https://www.jpe-innovations.com/precision-point/structural-damping-properties-mechanical-systems/`. Accessed: 2025-01-27.